Journal of Materials Chemistry C

ROYAL SOCIETY OF CHEMISTRY

PAPER

View Article Online
View Journal

Cite this: DOI: 10.1039/d5tc01562f

Improved performance of all-inorganic quantum-dot light-emitting diodes using an all-solution process at low temperatures†

Na Jia,‡[a] Yixuan Huang,‡[b] Mei-Yan Gao,*[c] Devika Laishram,[d] Dewei Chu,[b] Yongliang Zhang*[a] and Hui Yang*[e]

Received 16th April 2025,
Accepted 26th June 2025

DOI: 10.1039/d5tc01562f

rsc.li/materials-c

Organic light-emitting diode (OLED) displays have widespread applications, but the inherent instability of the devices, such as burn-in, short lifetime and poor stability, remains a critical drawback. Herein, an all-inorganic quantum-dot light-emitting diode (QLED) is developed using an all-solution process method at a low temperature. The simple strategy is engineered by introducing repeated UV-ozone treatments during Mg–NiO layer spin coating to enhance hole injection in the QLED device. The fabricated conventional QLED shows an improved EQE of 3.73%, which is 2.2 times higher than that of the QLED without UV-ozone treatment. In addition, the inverted all-inorganic LED exhibits a maximum EQE of 2.63% with a luminance of 3640 cd m^{-2}. It can be concluded that UV-ozone treatment creates non-stoichiometry in NiO, resulting in Ni^{3+} vacancy defects, which lower the valence band of Mg–NiO and enhance hole injection.

Introduction

Organic light-emitting diode (OLED) displays have found widespread applications in foldable smartphones and rollable TVs over the past 30 years because of their superior and unprecedented dark state, thin profile, and freeform factor.[1–3] However, OLEDs are composed of organic materials, resulting in inherent device instability, such as burn-in, short lifetime and poor stability.[4,5] Recently, quantum-dot light-emitting diodes (QLEDs) have led to breakthroughs in next-generation displays owing to the widely tunable emission, saturated color emission, and higher brightness of the QD emitter.[6,7] To date, the most efficient QLEDs are based on a hybrid architecture: anode/organic hole-transport layer (HTL)/QD emission layer/inorganic electron-transport layer (ETL)/cathode.[8,9] However, the sensitivity of organic HTLs to humidity and oxygen is still a problem for the practical application of QLEDs. For example, PEDOT:PSS serves as a hole injection layer (HIL), which can lead to the degradation of the device because it is acidic and easily causes corrosion of ITO.[10] PVK and TFB are widely used as HTLs in QLEDs, but the performance of these devices degrades over time, generally because of thermal instability and moisture- and/or oxygen-induced degradation.[11]

Nickel oxide (NiO) is one of the most widely used HTL materials owing to its optical transparency and excellent stability.[12,13] ZnO nanoparticles are commonly used in QLEDs as an ETL to achieve high efficiency because of their good electron transport capability and interfacial phase compatibility with the QD layer.[14,15] However, the device efficiency remains at a rather low level because of unbalanced charge injection and subsequent Auger recombination in the device, which is caused by the mismatch of the carrier mobilities and energy levels of inorganic HTLs and inorganic ETLs (*e.g.* ZnO has a higher electron mobility of 1.8×10^{-3} cm^2 V^{-1} s^{-1},[14] and NiO has a hole mobility of 2.5×10^{-4} cm^2 V^{-1} s^{-1} (ref. 16)), the morphology of the HTL, and the high barrier for hole injection from inorganic HTLs to QDs.[17,18] The deposition of the NiO layer normally requires very high annealing temperatures (over 250 °C) to synthesize NiO,[19–21] and this can cause damage to the active layers (QDs) and lead to the failure of LEDs. In addition, QLED devices are usually fabricated by several deposition techniques, including sputtering and ALD, which require expensive instruments and high temperature; especially, the preparation of the NiO layer has high costs.[22]

In this study, solution-deposited NiO and Mg-doped NiO nanoparticles are synthesized at a lower temperature to serve as an HTL to improve device efficiency and stability while

[a] School of Physics, CRANN and AMBER, Trinity College Dublin, Dublin D02PN40, Ireland
[b] School of Materials Science and Engineering, The University of New South Wales, Sydney, NSW 2052, Australia
[c] Department of Chemistry, University of California, Berkeley, California 94720, USA
[d] Department of Chemistry, Inha University, Incheon Metropolitan City, South Korea
[e] School of Electronic Engineering, Beijing University of Posts and Telecommunications, Beijing 100876, China

† Electronic supplementary information (ESI) available. See DOI: https://doi.org/10.1039/d5tc01562f

‡ Na Jia and Yixuan Huang contributed equally to this work.

maintaining the low cost of production. All-solution processed all-inorganic QLEDs are proposed, and a spin-coating process is used for the deposition of the HTL, emission layer and ETL in all-inorganic LEDs owing to its cost effectiveness, solution processability, high stability, and controllable morphologies and interface structures of thin films at the nanometer-length scale.[23,24]

The proposed devices include the conventional structure (ITO/Mg–NiO–NiO/QD/ZnO/Al) and inverted structure (ITO/ZnO/QD/Mg–NiO–NiO/Au). Introducing an Mg ion into the NiO lattice can increase the Ni vacancy (Ni^{3+}) concentration, thus enhancing the hole transport ability.[25] In addition, UV ozone (UVO) is applied on the Mg–NiO films during spin coating to increase the concentration of Ni^{3+} (NiOOH) on the surface and lower the film resistivity.[26,27] For an Mg–NiO layer with a thickness of about 40 nm, UV-ozone treatment can only act on the surface within a few nanometers.[28] Here, Mg–NiO is spin-coated four times, and UVO is applied after each spin coating. The NiO-based QLEDs are obtained by a facile spin-coating process in a natural environment and not in a glovebox. The inverted all-inorganic device demonstrates a high luminance of 14 785 cd m^{-2} and a low turn-on voltage of 3.1 V, the conventional device exhibits a maximum EQE of 3.73%, and the conventional device shows a peak EQE of 2.63% after UV-ozone treatment for 5 min.

Results and discussion

The transmission electron microscopy (TEM) image of CdSe/CdS QDs (Fig. 1(a)) reveals that the size of the QDs is around 5 nm. Because a simple synthesis protocol led to the formation of spherical and heterostructured QDs, the QDs are mostly spherical and exhibit only moderate size variations. The uniform size distribution and relatively defect-free structures of the QDs will guarantee pure color emission. XRD analyses evidence that the CdSe/CdS QDs have a wurtzite structure (Fig. S1, ESI†), indicating the epitaxial growth of a CdS shell on a wurtzite CdSe core. The XRD pattern of QDs corresponds well with that of hexagonal CdS (JCPDS no. 77-2306). However, a shift to higher angles is observed for the QDs, and the main peaks are located between CdSe and CdS standard values. The nanostructure of the as-prepared NiO is confirmed by TEM; as shown in Fig. S2(a) (ESI†), NiO nanoparticles have a general size from 20 to 60 nm.

The stoichiometry of nickel oxide is further investigated using XRD measurements, as shown in Fig. S2(b) (ESI†). The positions of the diffraction peaks for stoichiometric nickel oxide (JCPDS card no. 87-0712) are referenced by vertical lines. The diffraction peaks at 37.7°, 43.7°, and 63.3° correspond to the (111), (200), and (220) planes of non-stoichiometric nickel oxide (NiO), respectively.[16] Compared to the reference Mg–NiO pattern in the X-ray diffraction data, the observed diffraction peaks at the (111), (200), and (220) planes are broader, indicating smaller crystallite size and increased full-width at half-maximum (FWHM). The strongest diffraction peak is observed for the (200) plane, which demonstrates that Mg–NiO NPs have already crystallized. The full width at half-maximum of the diffraction peak of the (200) plane increases from 2.5 to 4.7, indicating that the crystallite size of Mg–NiO will decrease, according to the Scherrer equation. The results obtained for the grain sizes are similar to those from TEM (Fig. 1(b)).

The corresponding EDS analysis of Mg–NiO exhibits the presence of O, Ni and Mg, as shown in Fig. 1(c), consistent with the chemical composition of Mg–NiO nanoparticles, apparent by the very intense Ni, O, and Mg peaks. The EDS signal of Mg is weaker in the film than those of other elements owing to the relatively low molar concentration of Mg in the Mg–NiO film. These results confirm that Mg-doped NiO nanoparticles have been synthesized.

For the all-inorganic QLED device with a typical multiple-layered structure, the diagram of the QLED structure is schematically shown in Fig. 2(a), considering the all-inorganic characteristic of the QLED device. Specifically, the multilayer structure consists of Al, ZnO, QDs, NiO/Mg–NiO and ITO, which serve as the cathode, ETL, emitting layer, HTL, and anode, respectively. Each functional layer is made by spin coating, except for the electrodes. Fig. 2(b) presents a cross-sectional scanning electron microscopy image of the fabricated all-inorganic QLED with the ITO/NiO–Mg/QDs/Zn–MgO/Al architecture. The distinct multilayer structure is clearly resolved, confirming the well-defined and uniform deposition of each functional layer. The transparent ITO substrate provides smooth-bottom contact, while the NiO–Mg layer (around 40 nm) forms a compact and continuous hole-transport layer

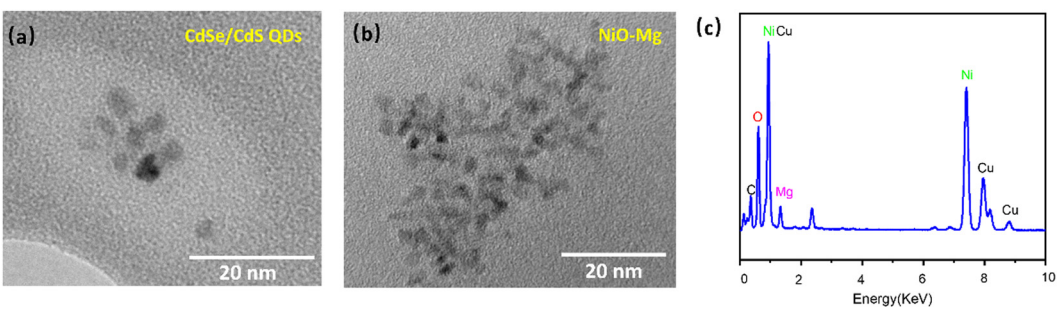

Fig. 1 TEM images of CdSe/CdS QDs (a) and Mg–NiO nanoparticles, (b) and the corresponding EDS analysis of NiO–Mg (c).

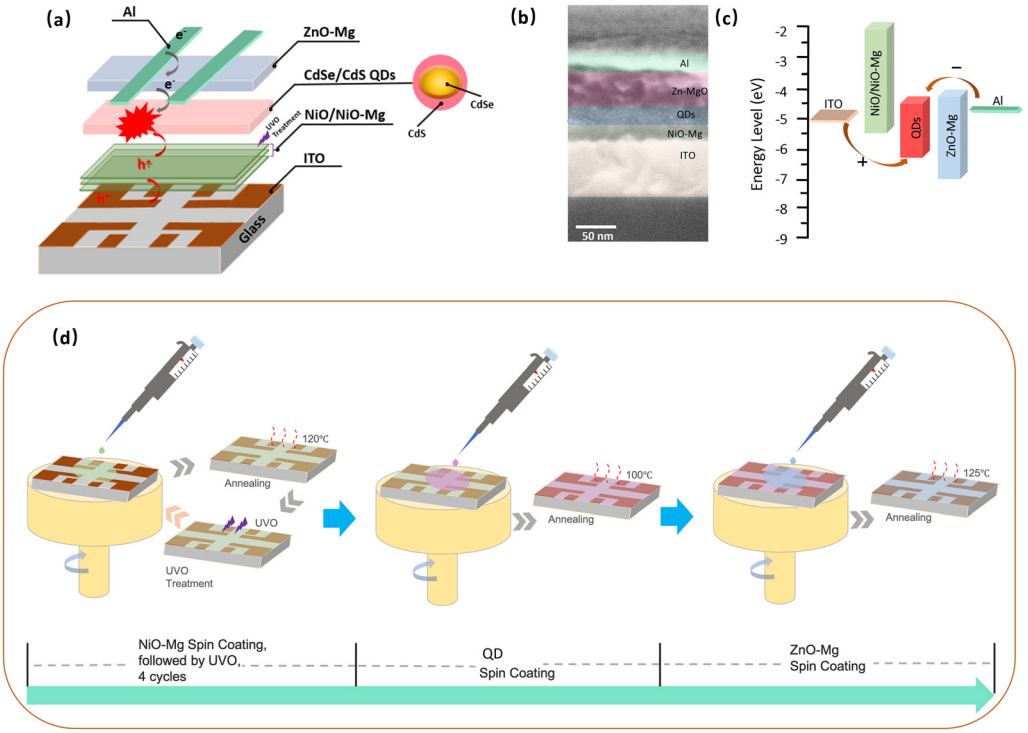

Fig. 2 (a) Conventional structure of the multilayer LED fabricated *via* spin coating. (b) Cross-sectional image of the LED device. (c) Energy level diagram of the functional layers in the device. (d) Schematic of LED device fabrication by spin coating.

(HTL), ensuring efficient hole injection. The quantum dot (QD) emission layer exhibits a uniform thickness (around 30 nm) with densely packed nanocrystals, which are crucial for high radiative recombination efficiency. The Zn–MgO layer serves as a robust electron transport and injection layer, demonstrating sharp interfaces with the QD and Al cathode layers, which facilitates balanced carrier injection and suppresses leakage currents. The energy levels of the functional layers of the QLED are shown in Fig. 2(c). The valence band edge and conduction band edge of NiO NCs are 1.8 eV and 5.1 eV,[29] respectively.

Fig. 2(d) shows a schematic illustration of the spin-coating process for the fabrication of the LED device, and the arrows indicate the phase transition during the whole process. The Mg–NiO solution is first spin-coated onto the patterned glass/ITO substrate and then annealed at 120 °C for 10 min in air, followed by UVO treatment (four cycles). Subsequently, the QDs dispersed in toluene are spin-coated on the glass/ITO/Mg–NiO substrate and annealed at 100 °C for 15 min in air. Finally, a ZnO–Mg methanol solution is further spin-coated onto the QD film and annealed at 125 °C for 10 min in air (for inverted LED fabrication, the ZnO–Mg solution is spin-coated first and NiO/Mg–NiO is spin-coated last).

Fig. 3 shows the schematic diagram of UVO treatment to explain the influence of UVO treatment on Mg–NiO particles.

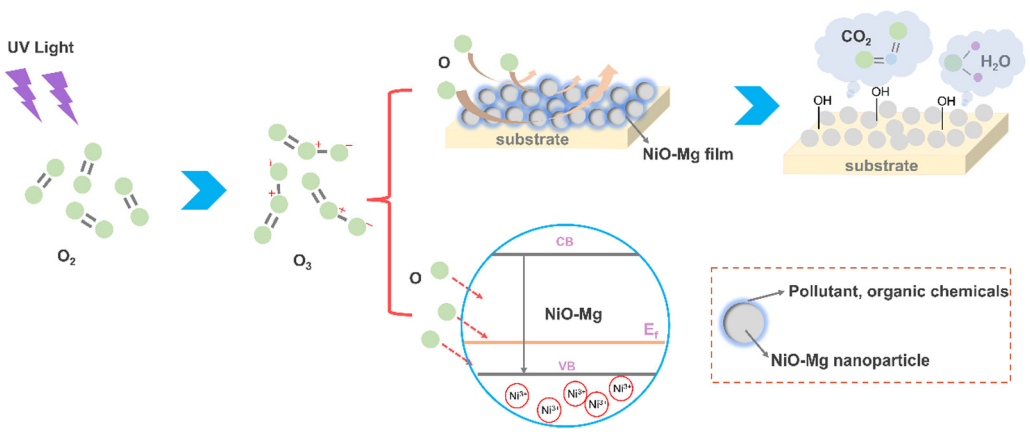

Fig. 3 Schematic of UVO treatment.

Free oxygen atoms are produced under ultraviolet irradiation in the UVO instrument, and ozone is synthesized when atomic oxygen reacts with oxygen (formula (1)). Then, the photo-oxidation reaction of UVO treatment happens on the surface of the Mg–NiO film. As illustrated in Fig. 3, UV rays and photogenerated reactive oxygen species (ROS), particularly atomic oxygen, interact with carbon- and nitrogen-containing contaminants adsorbed on the surface of Mg-doped nickel oxide (Mg–NiO) films, respectively. These surface-bound organic and inorganic residues undergo oxidative decomposition, resulting in the formation of volatile byproducts such as H_2O, CO_2, and various nitrogen oxides (NO_x). This photochemical cleaning process effectively removes insulating impurity layers, thereby decreasing the sheet resistance of the film and enhancing carrier transport properties in the cathode/HTL/QD structure and QD/HTL/anode structure. The improved carrier mobility contributes to the overall performance of the device, especially in optoelectronic applications, where interfacial purity is critical. This UV-assisted surface treatment methodology has been extensively adopted in a range of photoelectric devices to optimize the electronic conductivity and interface quality.[30] At the same time, hydroxyl radicals ($^{\bullet}OH$) are induced by UV-ozone treatment in the atmosphere, which are helpful for the next spin coating step for the formation of an even film because $^{\bullet}OH$ is one of the most highly reactive chemical species and can increase the surface energy and contact angle by forming OH groups.[31] In addition, oxygen atoms are induced into the internal structure of Mg–NiO nanoparticles; then, these oxygen species occupy pre-existing oxygen vacancy sites, effectively passivating such defects. After oxygen deficiencies are passivated, the transfer of holes from the Mg–NiO to QD layer is expected to occur much more smoothly.[32] The surface work function (WF) of Mg–NiO is dependent on the defect density and distribution on the surface.[33–35] In particular, oxygen-rich NiO with nickel vacancy defects exhibits enhanced p-type conductivity. UV-ozone exposure induces non-stoichiometry in the NiO lattice, generating Ni defects, which reduce electrical resistivity and elevate the WF.[26] An increased WF improves the energy level alignment between the Mg–NiO and QD layer, thereby facilitating hole injection and enhancing the overall hole mobility.

$$O_2 + O_2 \rightleftharpoons O_3 + O \quad (1)$$

XPS characterization was performed to conduct the chemical analysis of the prepared samples Mg–NiO-01, 02, 03 and 04. The HR XPS peaks in Fig. 4 were fitted using a Gaussian–Lorentzian function. The four samples 01, 02, 03 and 04 represent the lengths of time prepared Mg–NiO was exposed to UV-ozone treatment, with 01 being pristine at 0 min of exposure, followed by 3 min, 5 min and 8 min of exposure, respectively. The Mg 2p spectra (a, b, c and d) are fitted to two peaks with binding energies of around 49.0 eV and 50.4 eV, which can be assigned to MgO and $Mg(OH)_2$, respectively.

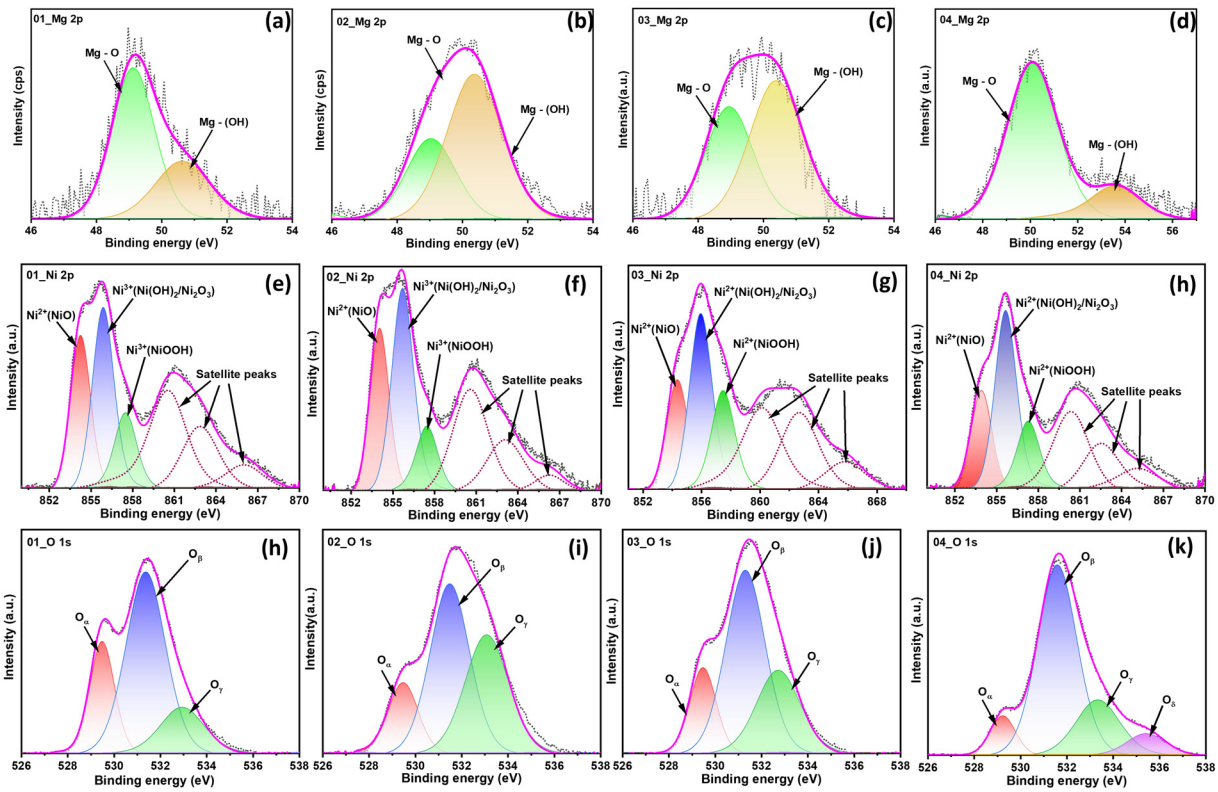

Fig. 4 HR XPS spectra of Mg 2p (a)–(d), Ni 2p (e)–(h), and O_{1s} (h)–(k) for Mg–NiO-01, 02, 03 and 04 (the prepared samples Mg–NiO-01, 02, 03 and 04 underwent UVO exposure for 0 min, 3 min, 5 min and 8 min, respectively).

However, Mg–NiO-04 shows peaks at 50.1 eV and 53.6 eV, respectively. The increase in the binding energy of Mg–NiO indicates a change in the chemical environment due to the oxidation process after longer exposure to UV-ozone (8 min). This can be observed from Fig. 4, where the % concentration of Mg–O is increased.

The Ni 2p peaks of all four materials are deconvoluted to three main peaks at binding energies of approximately 854, 855.7, and 857.5 eV, corresponding to NiO, $Ni(OH)_2/Ni_2O_3$, and NiOOH, respectively. The peaks at binding energies of approximately 860.6 eV, 862.5 eV, and 866 eV are assigned to satellite peaks. It can be observed from the data given in Table 1 that with increasing exposure time, the % concentration of Ni^{2+} decreases from 5.7% for unexposed Mg–NiO-01 to 2.1% for Mg–NiO-04 exposed for 8 min. Additionally, the Ni^{3+}/Ni^{2+} ratio, as given in Table 1, indicates an increase in Ni^{3+}, which can be due to the transformation of Ni^{2+} to Ni^{3+}. This is a result of the increase in the number of Ni vacancies with increasing UV-ozone exposure time and hence results in the enhanced formation of Ni^{3+} to compensate for Ni vacancies, sustaining the electroneutrality of the material. The enhancement in Ni^{3+} is important for increasing the hole transport mobility in devices. The enhancement in Ni vacancies also changes the % concentration of oxygen, which increases from 48% for pristine Mg–NiO-01 to 57% for Mg–NiO-04. The O_{1s} spectrum is deconvoluted into three components at 529.5 eV, 531.5 eV, and 533.0 eV, corresponding to lattice oxygen (O_α), oxygen vacancies (O_β), and surface-adsorbed hydroxyl groups (O_γ), respectively. Mg–NiO-04 has an additional O_δ peak at 535.4 eV due to the presence of moisture.

In addition, the SEM images of the surface morphologies of the functional layers are shown in Fig. S3(a)–(d) (ESI†). As can be clearly seen in Fig. S3(a) (ESI†), the NiO film coated on ITO/glass exhibits a fully covered surface morphology with well-crystallized and large grains; however, there are some microholes. They may originate from the large size of NiO particles and the post-annealing process after spin coating. It is apparent that Mg–NiO shows a well-formed (Fig. S3(b), ESI†) film, and the substrate is fully covered by the Mg–NiO film, which is beneficial for the deposition of the QD layer and carrier transmission. The CdSe/CdS QD film, fabricated by spin coating on the glass/ITO/Mg–NiO substrate, also exhibits a uniform morphology without any pinholes (Fig. S3(c), ESI†). This can indeed reduce the number of current shunting pathways and enhance charge collection efficiency. The small grain size of the QD film can result in fewer grain boundaries, which is favorable for achieving higher efficiency because boundaries in emission films cause undesirable charge recombination at their associated charge trap states.[36,37] After spin coating the ZnO–Mg ethanol solution onto the QD film, the film quality is further improved, with a higher coverage and no pinholes, as can be witnessed in Fig. S3(d) (ESI†).

Using the hole-only device architecture (ITO/NiO or NiO–Mg/Al) (Fig. S4(a), ESI†) and the corresponding log–log J–V characteristics shown in Fig. S4(b) (ESI†), the impact of UV-ozone treatment on hole transport can be clearly evaluated. Notably, the pristine NiO device shows a lower current density than the NiO–Mg devices, and progressive increase in the UVO treatment time from 0 to 5 minutes systematically increases the current density at a given voltage. This trend implies that UVO treatment further passivates oxygen vacancies and improves the film stoichiometry, thereby boosting hole mobility and lowering the trap density. The rightward shift of the transition voltage after UVO exposure provides additional evidence of more efficient hole transport. Such improved hole-only device performance confirms that the combined effect of Mg doping and UVO treatment enhances hole injection and transport, supporting the improvement in QLED performance by achieving better carrier balance and suppressing efficiency roll-off.

As shown in Fig. 5(a), the current density–voltage–luminance (J–V–L) curves reveal that moderate UVO treatment significantly improves carrier injection and recombination efficiency. Specifically, the turn-on voltage, defined at a luminance of 1 cd m^{-2}, decreases from 3.8 V for the pristine NiO device to 3.1 V for the device with 5 min UVO-treated Mg–NiO, implying a lower hole injection barrier owing to the enhanced energy level alignment and surface passivation. Consistently, the operating voltage required to reach a luminance of 1000 cd m^{-2} decreases from 5.2 V (pristine NiO) to 4.5 V (5 min UVO-treated Mg–NiO), highlighting improved hole transport and balanced charge injection. Furthermore, the maximum luminance substantially increases from 8200 cd m^{-2} for the untreated NiO-based device to 14 785 cd m^{-2} for the optimally treated sample, confirming that the improved interfacial properties facilitate more efficient radiative recombination. However, when the UVO exposure time increases to 8 min, the peak luminance and EQE drop to 8642 cd m^{-2} and 2.51%, respectively. This degradation can be attributed to

Table 1 HR XPS analysis of Mg–NiO exposed to UVO for different times

		Mg_NiO_01		Mg_NiO_02		Mg_NiO_03		Mg_NiO_04	
		Conc. (%)	Position	Conc. (%)	Position	Conc. (%)	Position	Conc. (%)	Position
O 1s	O_α	11.5	529.5	6.3	529.5	10.0	529.5	5.0	529.2
	O_β	29.6	531.4	19.7	531.5	31.5	531.3	37.0	531.6
Ni $2p_{2/3}$	Ni^{2+} (NiO)	5.3	854.2	2.7	854.0	3.2	854.4	2.1	853.9
	Ni^{3+} (Ni_2O_3)	6.2	855.9	3.4	855.7	4.9	855.9	3.6	855.6
Ni^{3+}/Ni^{2+}		1.17		1.26		1.53		1.71	
Ni/O		0.49		0.29		0.33		0.20	

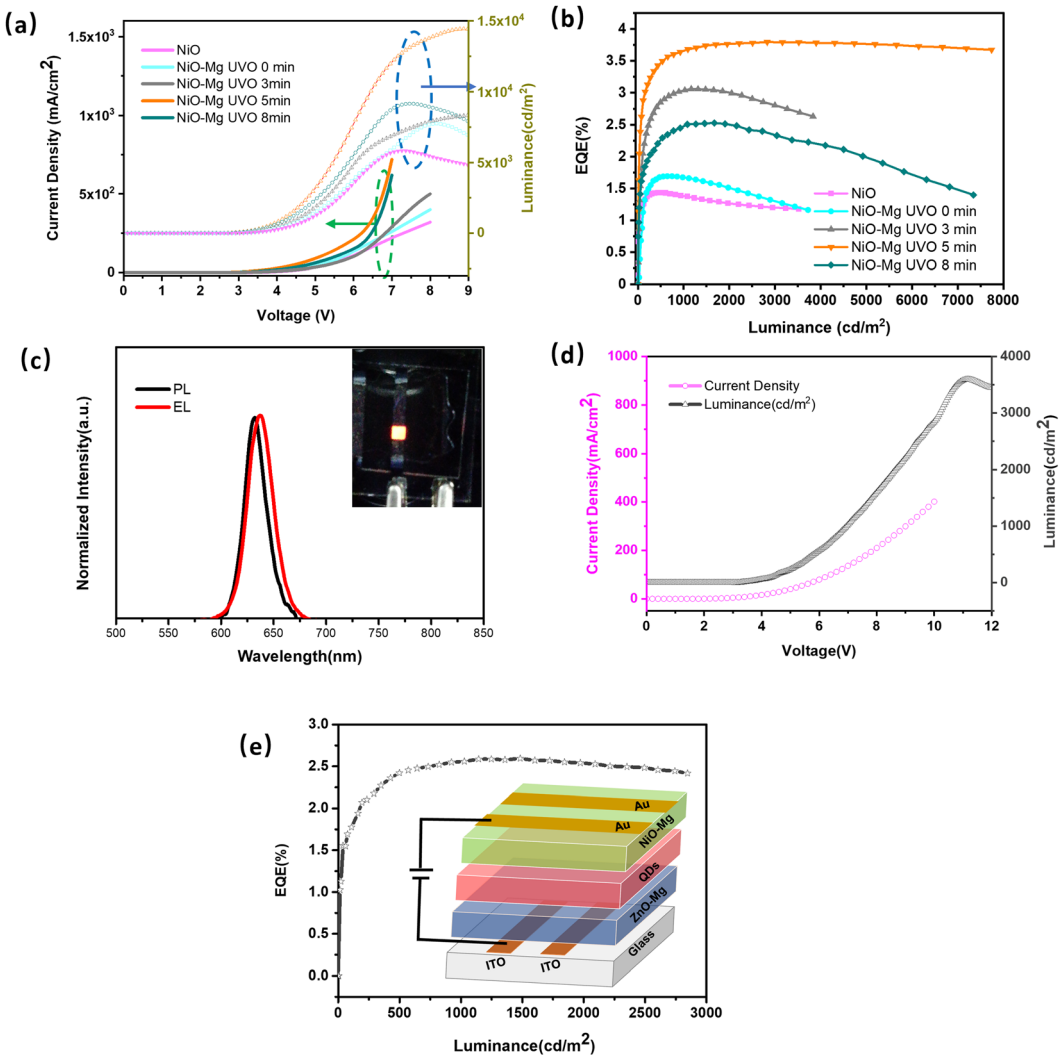

Fig. 5 Comparison of the EL performance of the LEDs with different UVO exposure times: (a) ηA–J–ηEQE and (b) J–V–L. (c) PL characteristics of all-inorganic QLEDs with the ITO/NiO(Mg–NiO)/QDs/ZnMgO/Al structure. Representative (d) J–V–L and (e) EQE–L characteristics of the inverted all-inorganic QLEDs.

excessive oxygen adsorption and interstitial formation in the Mg–NiO lattice, leading to increased trap states and non-radiative recombination centers.[38]

Fig. 5(b) presents the external quantum efficiency (EQE) as a function of luminance for samples under different UVO conditions. The device with 5 min UVO treatment exhibits the highest peak EQE of 3.73%, compared to 1.38% for the pristine NiO device and 1.69% for the as-deposited Mg–NiO without UVO. Importantly, the EQE roll-off at a high luminance is significantly suppressed in the optimally treated device: at 3000 cd m^{-2}, the EQE remains ~3.6%, which is twice that of the untreated device at the same luminance. This indicates that the optimized UVO treatment effectively mitigates charge imbalance and reduces non-radiative loss pathways at high injection currents. The normalized photoluminescence (PL) and electroluminescence (EL) spectra in Fig. 5(c) show that the emission peak remains centered at 627 nm with a narrow full width at half-maximum (FWHM) of ~28 nm, exhibiting a negligible spectral shift caused by the quantum-confined Stark effect and excellent color purity under electrical excitation.[39] This demonstrates the high optical quality of the QDs and the spectral stability of the device under different driving conditions.

To confirm the general applicability of the UVO treatment strategy, Fig. 5(d) and (e) present the J–V–L and EQE–L characteristics of an inverted-architecture device (ITO/ZnO–Mg/QDs/Mg–NiO/Au). The inverted device with a 5 min UVO-treated Mg–NiO layer achieves a turn-on voltage of 3.3 V and a maximum luminance of 3640 cd m^{-2}, with a peak EQE of 2.63%. The roll-off trend in the inverted configuration is also improved, with the EQE remaining at 2.3% at 2000 cd m^{-2}, corroborating that the UVO-induced modulation of the Mg–NiO layer effectively enhances hole injection and stabilizes performance irrespective of the device polarity. This systematic comparison confirms that an appropriate UVO treatment duration (5 min) optimally tunes the Mg–NiO interfacial properties, significantly reducing turn-on and operating voltages, enhancing the luminance, and effectively suppressing the efficiency

roll-off at high brightness for conventional and inverted all-inorganic QLEDs. This demonstrates the promising potential of UVO-assisted Mg–NiO layers in realizing high-performance solution-processed QLEDs.

Conclusions

In summary, we report a simple strategy by introducing repeated UV-ozone treatments to enhance the hole injection for QLED. Conventional and inverted QLEDs are fabricated using spin coating for each functional layer, and we demonstrate that the device performance can be promoted by repeated UV-ozone treatments for 5 min, which lowers the barrier between the HTL and QDs. The fabricated conventional QLED shows an improved EQE of 3.73%, which is 2.2 times higher than that of the device without UV-ozone treatment. In addition, the inverted all-inorganic LED exhibits a maximum EQE of 2.63% with a luminance of 3640 cd m^{-2}; this performance is also improved compared to that of the reported one (the efficiency of an inverted all-inorganic LED and the maximum luminance of the device are 0.25% and 1400 cd m^{-2}).[40] Based on all observations, it can be concluded that UV-ozone treatment creates non-stoichiometry in NiO, resulting in Ni^{3+} vacancy defects, which lower the valence band of Mg–NiO and enhance hole injection.

Conflicts of interest

The authors declare no conflicts of interest.

Data availability

The data supporting the findings of this study are available from the corresponding author upon reasonable request. All raw data, including device performance, UV-ozone treatment procedures, and characterization results, have been archived and can be provided to ensure transparency and reproducibility.

Acknowledgements

This work was supported by Science Foundation Ireland 18/EPSRC-CDT-3581 and the Engineering and Physical Sciences Research Council EP/S023259/1. The authors also acknowledge financial support from the Australian Research Council Projects LP210200495, LP190100829, and DP210100879.

References

1 J.-H. Lee, C.-H. Chen, P.-H. Lee, H.-Y. Lin, M.-K. Leung, T.-L. Chiu and C.-F. Lin, *J. Mater. Chem. C*, 2019, **7**, 5874–5888.
2 A. Buckley, *Organic light-emitting diodes (OLEDs): materials, devices and applications*, Elsevier, 2013.
3 Y. Huang, E.-L. Hsiang, M.-Y. Deng and S.-T. Wu, *Light: Sci. Appl.*, 2020, **9**, 105.
4 H. Guo, Q. Peng, X.-K. Chen, Q. Gu, S. Dong, E. W. Evans, A. J. Gillett, X. Ai, M. Zhang and D. Credgington, *Nat. Mater.*, 2019, **18**, 977–984.
5 Y. Hattori, T. Kusamoto and H. Nishihara, *Angew. Chem., Int. Ed.*, 2015, **54**, 3731–3734.
6 H. Yu, H. Zhu, M. Xu, J. Zhang, H. Feng, L. Zhang, S. Liu and W. Xie, *ACS Photonics*, 2022, **10**, 2192–2200.
7 M. Yang, L. Xie, Y. Q. Q. Yi, Y. Liu, X. Meng, W. Su and Z. Cui, *Adv. Mater. Technol.*, 2023, **8**, 2202105.
8 H. Zhang, X. Sun and S. Chen, *Adv. Funct. Mater.*, 2017, **27**, 1700610.
9 B. S. Mashford, M. Stevenson, Z. Popovic, C. Hamilton, Z. Zhou, C. Breen, J. Steckel, V. Bulovic, M. Bawendi and S. Coe-Sullivan, *Nat. Photonics*, 2013, **7**, 407–412.
10 S. Ahn, S. H. Jeong, T. H. Han and T. W. Lee, *Adv. Opt. Mater.*, 2017, **5**, 1600512.
11 X. Yang, Y. Ma, E. Mutlugun, Y. Zhao, K. S. Leck, S. T. Tan, H. V. Demir, Q. Zhang, H. Du and X. W. Sun, *ACS Appl. Mater. Interfaces*, 2014, **6**, 495–499.
12 J. Caruge, J. E. Halpert, V. Wood, V. Bulović and M. Bawendi, *Nat. Photonics*, 2008, **2**, 247–250.
13 V. Wood, M. J. Panzer, J.-M. Caruge, J. E. Halpert, M. G. Bawendi and V. Bulovic, *Nano Lett.*, 2010, **10**, 24–29.
14 Y.-L. Shi, F. Liang, Y. Hu, M.-P. Zhuo, X.-D. Wang and L.-S. Liao, *Nanoscale*, 2017, **9**, 14792–14797.
15 L. Qian, Y. Zheng, J. Xue and P. H. Holloway, *Nat. Photonics*, 2011, **5**, 543–548.
16 R. Vasan, H. Salman and M. Manasreh, *IEEE Electron Device Lett.*, 2018, **39**, 536–539.
17 K.-S. Cho, E. K. Lee, W.-J. Joo, E. Jang, T.-H. Kim, S. J. Lee, S.-J. Kwon, J. Y. Han, B.-K. Kim and B. L. Choi, *Nat. Photonics*, 2009, **3**, 341–345.
18 Z. Wang, P. K. Nayak, J. A. Caraveo-Frescas and H. N. Alshareef, *Adv. Mater.*, 2016, **28**, 3831–3892.
19 B. S. Mashford, T.-L. Nguyen, G. J. Wilson and P. Mulvaney, *J. Mater. Chem.*, 2010, **20**, 167–172.
20 K. X. Steirer, J. P. Chesin, N. E. Widjonarko, J. J. Berry, A. Miedaner, D. S. Ginley and D. C. Olson, *Org. Electron.*, 2010, **11**, 1414–1418.
21 H. Wang, H. Yuan, J. Yu, C. Zhang, K. Li, M. You, W. Li, J. Shao, J. Wei and X. Zhang, *ACS Appl. Mater. Interfaces*, 2020, **12**, 53528–53536.
22 Q. Xu, X. Li, Q. Lin, H. Shen, H. Wang and Z. Du, *Front. Chem.*, 2020, **8**, 265.
23 J. Kwak, W. K. Bae, D. Lee, I. Park, J. Lim, M. Park, H. Cho, H. Woo, D. Y. Yoon and K. Char, *Nano Lett.*, 2012, **12**, 2362–2366.
24 Q. Shan, J. Li, J. Song, Y. Zou, L. Xu, J. Xue, Y. Dong, C. Huo, J. Chen and H. Zeng, *J. Mater. Chem. C*, 2017, **5**, 4565–4570.
25 W. H. Jung, B. J. Kim, M. Choi, H. Lee, H. Cho, Y. W. Kwon, Y. Choi, H. G. Lee, J. Yoon, K. Lee, S. H. Oh, S. Y. Cho, D. C. Lee, S. Jeong and J. Lim, *Adv. Mater.*, 2024, **36**, 2410441.
26 R. Islam, G. Chen, P. Ramesh, J. Suh, N. Fuchigami, D. Lee, K. A. Littau, K. Weiner, R. T. Collins and K. C. Saraswat, *ACS Appl. Mater. Interfaces*, 2017, **9**, 17201–17207.

27 Y. Jiang, L. Jiang, F. S. Yan Yeung, P. Xu, S. Chen, H.-S. Kwok and G. Li, *ACS Appl. Mater. Interfaces*, 2019, **11**, 11119–11124.
28 K. Efimenko, W. E. Wallace and J. Genzer, *J. Colloid Interface Sci.*, 2002, **254**, 306–315.
29 F. Wang, Z. Wang, X. Zhu, Y. Bai, Y. Yang, S. Hu, Y. Liu, B. You, J. Wang and Y. Li, *Small*, 2021, **17**, 2007363.
30 R. Kohli and K. Mittal, *Developments in Surface Contamination and Cleaning: Applications of Cleaning Techniques*, Elsevier, 2018, Vol 11.
31 P. Yue, *Chem. Eng. Sci.*, 1993, **48**, 1–11.
32 D. Li, W. Qin, S. Zhang, D. Liu, Z. Yu, J. Mao, L. Wu, L. Yang and S. Yin, *RSC Adv.*, 2017, **7**, 6040–6045.
33 A. Janotti and C. G. Van de Walle, *Phys. Rev. B: Condens. Matter Mater. Phys.*, 2007, **76**, 165202.
34 D. C. Look, J. W. Hemsky and J. Sizelove, *Phys. Rev. Lett.*, 1999, **82**, 2552.
35 L. Halliburton, N. Giles, N. Garces, M. Luo, C. Xu, L. Bai and L. A. Boatner, *Appl. Phys. Lett.*, 2005, 87.
36 X. Liu, Z. Liu, H. Ye, Y. Tu, B. Sun, X. Tan, T. Shi, Z. Tang and G. Liao, *Electrochim. Acta*, 2018, **288**, 115–125.
37 D. Bai, J. Zhang, Z. Jin, H. Bian, K. Wang, H. Wang, L. Liang, Q. Wang and S. F. Liu, *ACS Energy Lett.*, 2018, **3**, 970–978.
38 Y. Ka, E. Lee, S. Y. Park, J. Seo, D.-G. Kwon, H. H. Lee, Y. Park, Y. S. Kim and C. Kim, *Org. Electron.*, 2013, **14**, 100–104.
39 J.-M. Caruge, J. E. Halpert, V. Bulović and M. G. Bawendi, *Nano Lett.*, 2006, **6**, 2991–2994.
40 B. Ghosh and N. Shirahata, *Crystals*, 2019, **9**, 385.